3D Simulation of Seismic Noise in a Sedimentary Basin with a Blind Fault Structure: Application to the Sensitivity of Surface H/V and Noise Array Measurements

David Gregor[1], Emmanuel Chaljub[1], Marc Wathelet[1], Fabrice Hollender[1,2], Vincent Perron[1,2]

[1]ISTerre, Grenoble Alpes University, France, [2]CEA, Cadarache, France

Abstract

We have developed a 3D computational tool to synthesize ambient seismic vibration (ASV) wavefields due to surface noise sources. We have applied this tool to a set of receivers located around a blind fault, in a canonical model of the Mygdonian sedimentary basin in Greece. We present the results of several analyses of synthetic noise seismograms (up to 5 Hz) corresponding to many different source-receiver configurations. We further focus on two different analyses: single-station H/V, which are compared to the predictions obtained in the Diffusive Field Approximation (DFT), and noise array measurements.

Processing part of the ASV tool

The main goal of the processing part of the ASV tool is to obtain noise, synthetic seismograms due to spatial and temporal distribution of noise sources. In order to do that and to avoid running a numerical wave propagation simulation each time after changing spatial and/or temporal property of noise source, we use here the recipe (originally presented in the notes of Ampuero 2003) based on the concept of the reciprocity theorem and Green's functions. This recipe is particularly advantageous if one assumes that number of noise sources N_{sour} is much larger than the number of receivers N_{rec}.

In the first stage of the processing part, we need to calculate set of synthetic Green's functions. This can be summarized in the following steps:

- select a numerical method for the wavefield simulation, e.g. spectral element method implemented in the computer code EFISPEC3D (De Martin 2011, Chaljub et al. 2015, Maufroy et al. 2015),
- mesh the proposed computational model (Fig. 3) by the hexahedra elements (Fig. 4a),
- select coordinate position of one receiver from array of receivers on the free-surface (Fig. 4b),
- run 3 independent wavefield simulations (Fig. 4c) with the single force source applied to position of the selected receiver. Each of 3 simulations corresponds to different orientation of the single force (F_x, F_y, F_z) with source-time function (stf) of dirac-delta like function (f.k.a impulse source),
- calculate the resulting 3 component Green's function in every Gauss-Lobatto-Legendre (GLL) point at the free surface for all 3 simulations (Fig. 4c) – set of Green's functions,
- apply decimation in time (proposed by De Martin et al. 2013) on each component of Green's function using the finite impulse response (FIR) filter during the simulation and infinite impulse response (IIR) after the simulation in order to reduce binary file size of the set of Green's functions (Fig 5.).
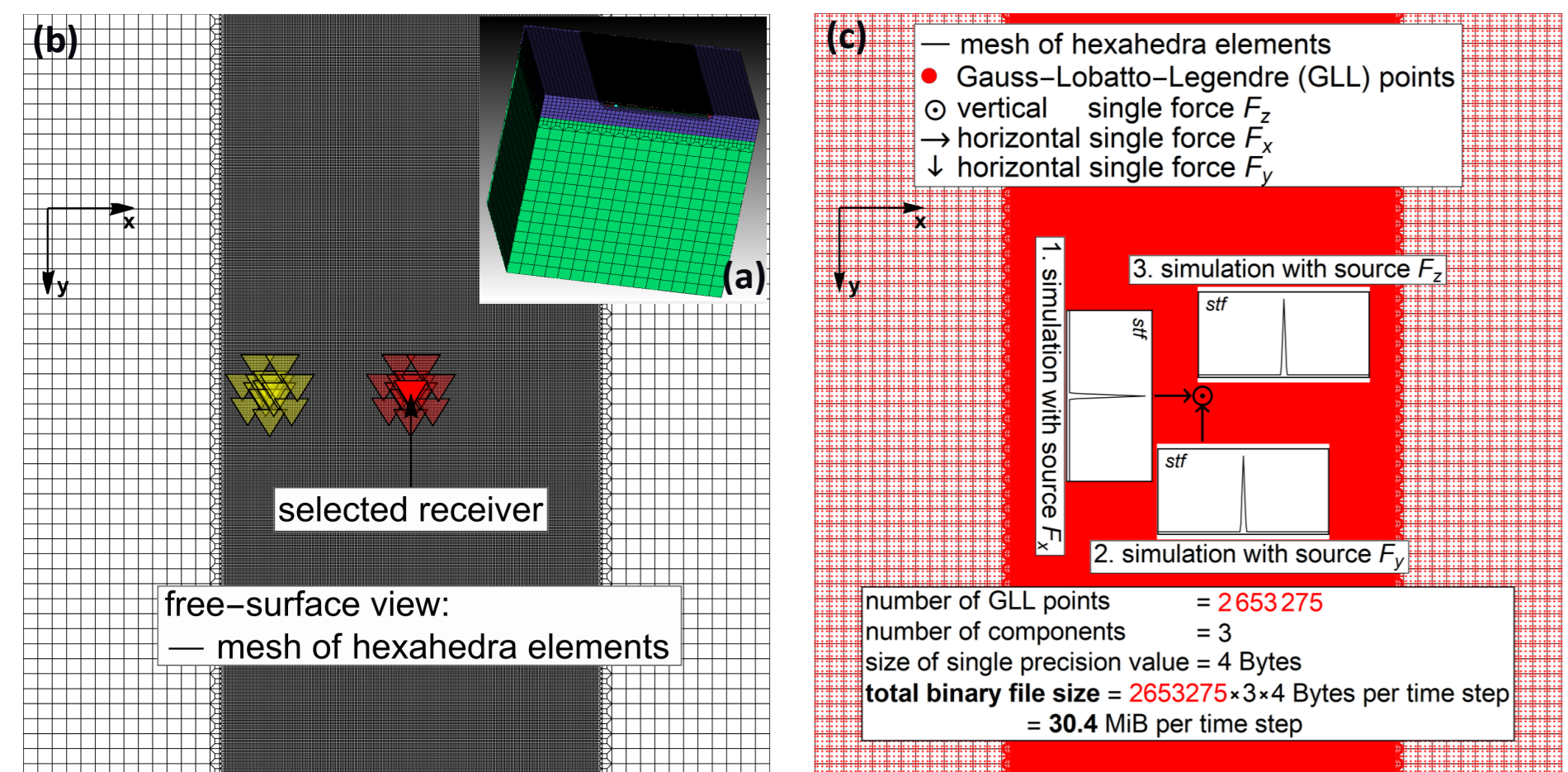

Figure 4. (a) Hexahedron mesh of the computational model. (b) The free-surface view of the meshed computational model with highlighted position of selected receiver. (c) Illustration of an application of single force source at position of selected receiver, together with the positions of all free surface GLL points. The table inside the figure provides binary size per time step information if non-decimated 3 component Green's functions are stored in the GLL points at the free-surface.

In the second stage of the processing part we prepare desired configuration of noise sources (illustration in Fig. 6). The configuration of noise sources consists of selecting the region on the free-surface where noise sources are located and selecting their spatial and temporal properties.

In order to generate noise wavefield, we use multiple single force sources. Each of them acts at one point of the free-surface with random value of its spatial and temporal property – point location within the region, arbitrary amplitude, orientation of a force (f_x, f_y or f_z) and time-delay of prescribed source-time function (stf).
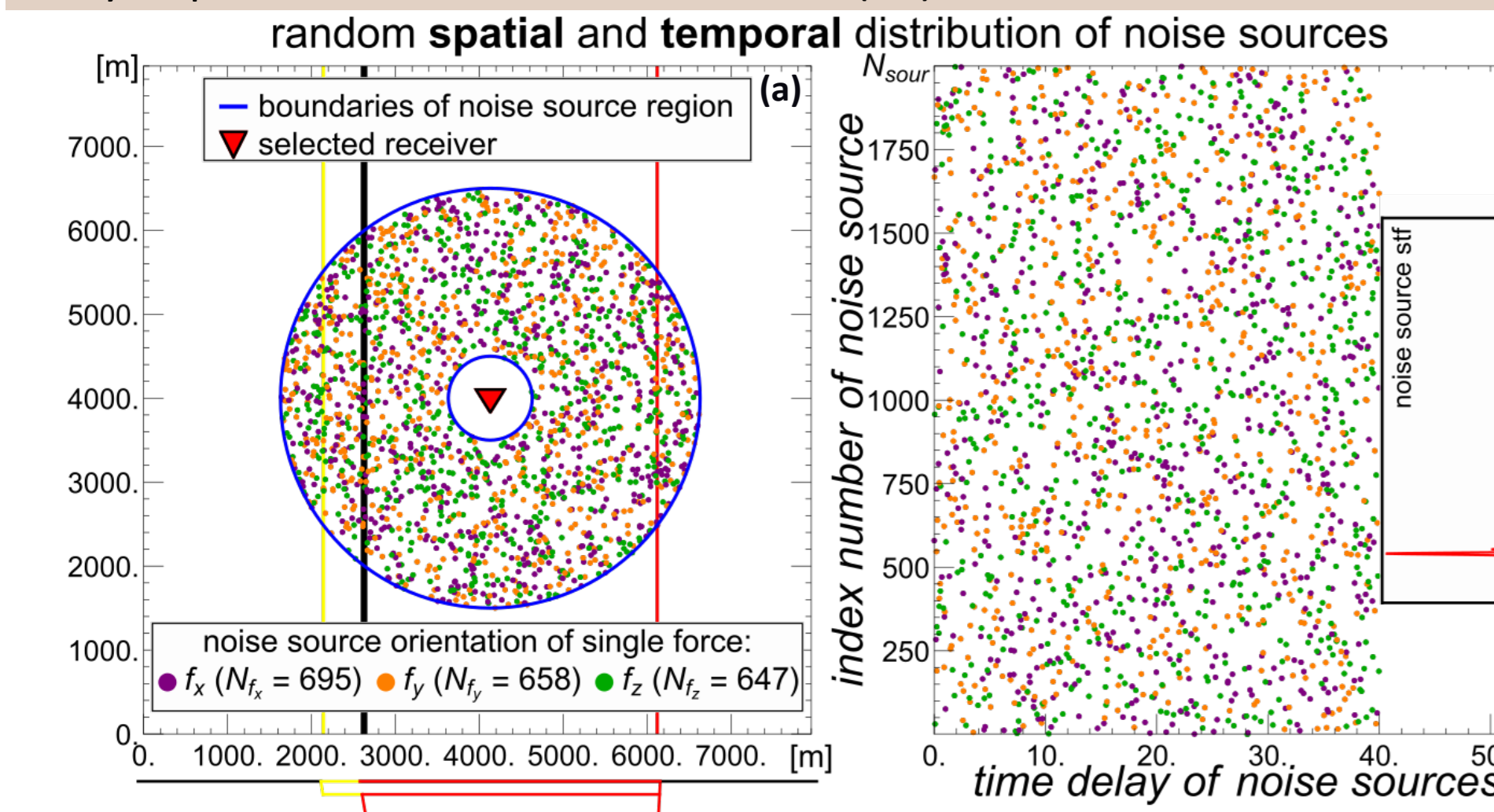

Figure 6. The illustration of one realization (e.g. one random seed) of random spatial and temporal properties of noise sources: (a) The selected receiver surrounded by $N_{sour} = 2000$ single force noise sources (purple, orange, green dots) with different force orientation with unitary amplitude within the area bounded by 2 concentric circles. (b) The values of time shift of stf (pictured in the small frame) corresponding to index of single force noise source $\{1,...,N_{sour}\}$.

In the last stage of the processing part, we use the reciprocity theorem which shows that for any wavefield we can switch between the receiver and source positions without changing the values of the observed wavefield. This means that wavefield at a point $\vec{r}$ generated by a point source located at a point $\vec{s}$ is equal to the wavefield at a point $\vec{s}$ generated by a point source located at point $\vec{r}$:

$$G_{ij}(\vec{r} \mid \vec{s}) = G_{ji}(\vec{s} \mid \vec{r})$$

Since we have set of Green's functions for all GLL points on the free-surface, we can interpolate the values of Green's function for any point on the free-surface and this gives us the freedom of choosing any position of the source. Afterwards, we can prepare the Green's tensor for all desired noise sources and convolve it with the corresponding noise source-time function in order to obtain final noise seismograms.

Post-processing part of the ASV tool
Single station method - H/V spectral ratio

In the case of H/V analysis, we have calculated noise seismograms for 4 selected receivers from the arrays of receivers due to noise sources located in the region of the basin, in the region at the right part of the bedrock and in the region at the left part of the bedrock (Fig. 7b).

For each receiver we obtained 1000 noise seismograms due to 1000 different realizations of noise sources spatial and temporal properties. This allows us to calculate statistical values (median μ and standard deviation σ) on set of 1000 H/V curves (Fig. 7a).

We compared the median curve of H/V curves with the theoretical H/V curve based on the 1D elastic H/V diffuse field theory (DFT) assumption (Fig. 7a). For calculation we use tool HV-Inv developed by García-Jerez & Piña Flores (García-Jerez et al. 2016, Piña-Flores et al. 2017), which allows us to compute the theoretical H/V curve for a receiver on a free-surface of 1D horizontally layered medium by assuming diffuse seismic wavefield. Since some parts of our model (e.g. middle of the shallow & deep part of the basin) can be considered as a model with only 1D vertical material dependence, we used elastic material parameters of layers to calculate the 1D theoretical H/V curve based on the elastic DFT assumption.
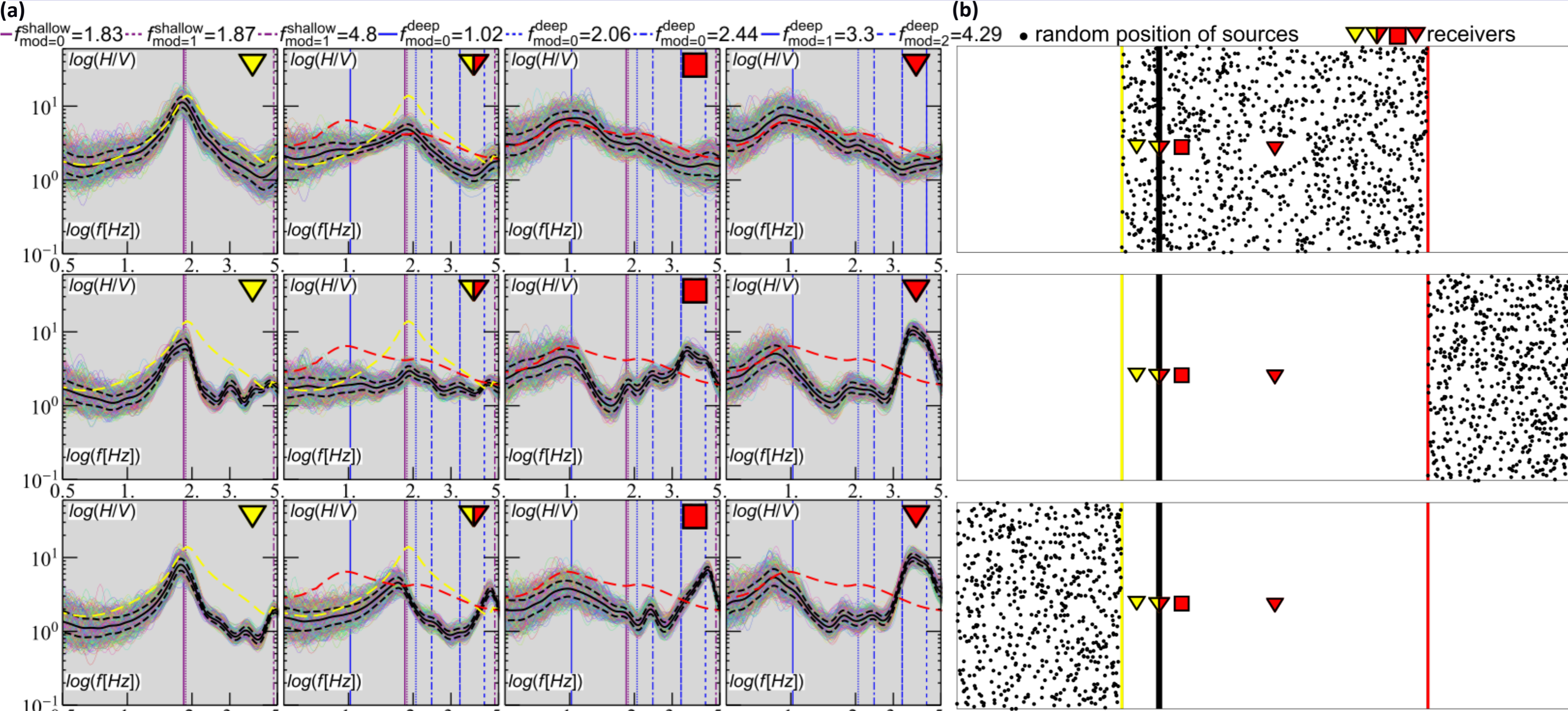

Figure 7. (a) The results of H/V analysis of 1000 synthetic noise seismograms of the 4 representative receivers (4 columns of panels) corresponding to 3 different distinct regions of noise sources (3 rows of panels). Each panel contain the 1000 H/V curves of different colours, the statistical measures in black color and two H/V curves (yellow & red) based on the DFT assumption corresponding to 1D profile in the shallow and deep part of the basin. The vertical segment represent maximum frequencies of the theoretical ellipticity curves of Rayleigh Modes. (b) The illustration of the 3 different noise source regions – noise sources within the region of only the basin, of only the right part of the bedrock or only the left part of the bedrock. Each of 1000 realizations ensures random temporal and spatial properties of noise sources but within the bounds of corresponding regions.

Motivation

The use of ASV has become an important tool for seismic hazard assessment, especially in regions of low-to-moderate seismic activity. Indeed, ASV has been used in the last decades to provide valuable information about the structure of the Earth at different scales using post-processing single station methods (e.g. H/V spectral ratio), two station method (e.g. noise-based standard spectral ratio and cross-correlation) or many station method (e.g. frequency-wavenumber $f - k$ analysis).

Despite recent progress in analysis of ASV, some questions remain unanswered, such as the question of the origin of the processes that cause time variations of subsurface properties (which are possibly related to the modification within the ambient vibration wavefield composition) retrieved by ASV analyses in terms of the H/V peak frequency f_0.

The time variation of the subsurface properties was observed through H/V analysis of a peak frequency f_0 corresponding to the real ASV measurements at the cross-sectional profile of local, heterogenous sedimentary structure in the Mygdonian basin in Greece (Fig. 1). Hollender (2019) have shown strong variation of f_0 as a function of time. By processing the ASV measurements carried out over a period of 3h for a station located at the cross-sectional profile above the blind fault, they have shown that the value of f_0 for the first 3h of measurements in Fig. 2(a) is different from the value of f_0 for the last 1h of measurements in Fig. 2(b). This means that one can observe clear shift of f_0 with respect to time. The possible explanation based on Hollender (2019) might lie in the different position of noise sources and corresponding propagation direction of the surface waves:

- the noise sources located in the North (Fig. 2a) generate wavefield propagating southward and the recorded H/V signature might correspond to the thickness of sedimentary layer to the North with f_0 near 2 Hz,
- however, the noise sources located in the South (Fig. 2b) generate wavefield propagating northward and the recorded H/V signature might correspond to the thickness of sedimentary layer to the South with f_0 near 1 Hz.
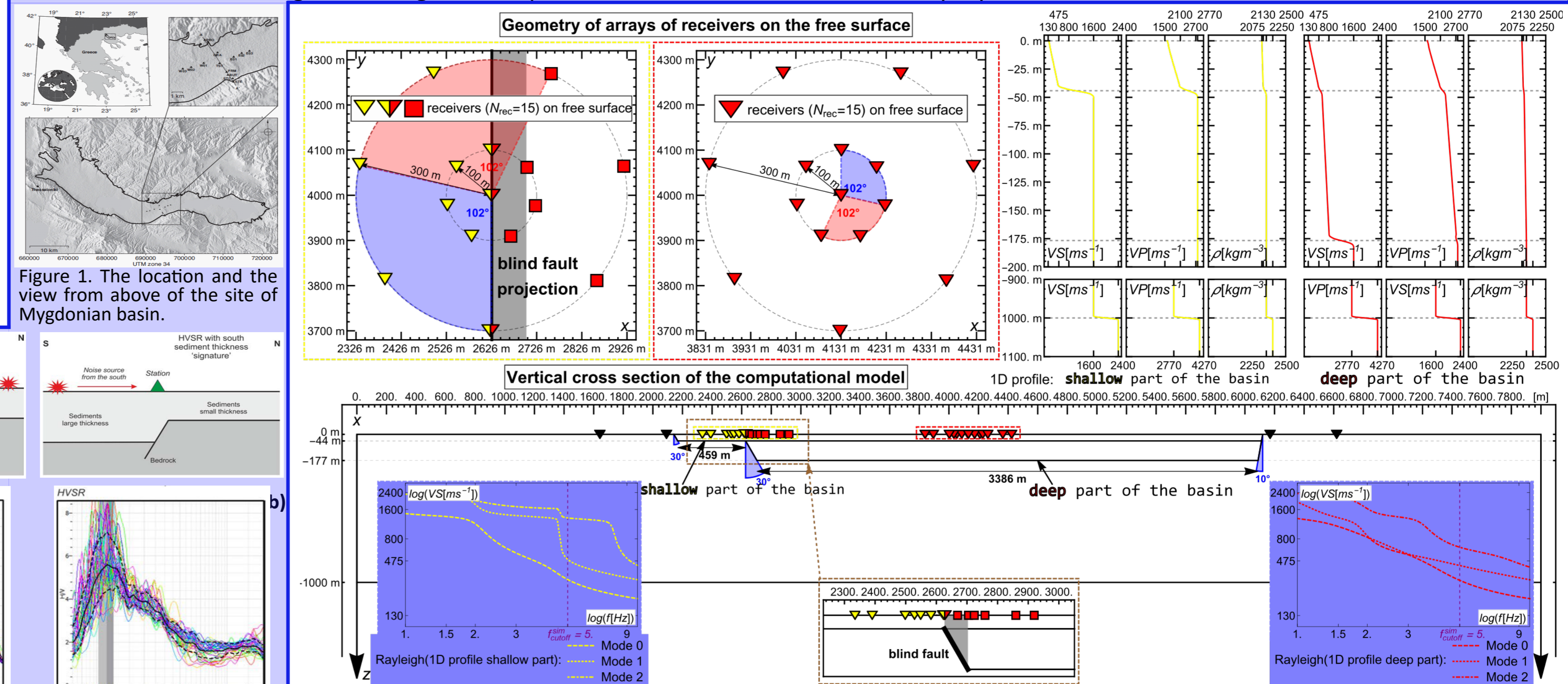

Figure 1. The location and the view from above of the site of Mygdonian basin.

Figure 2. (a, b) The strong variation of the H/V response (lower figures) at the station (denoted as green triangle) above blind fault within the Mygdonian basin (upper figures) and possible explanation of the time shift of peak frequency of the H/V related to the position of sources (denoted as red star) and propagation direction of the ambient vibration wavefield (Hollender 2019).

Figure 3. The computational model based on the simplified 3D model of the Mygdonian basin with stair-step geometry representing the blind fault. The free-surface of the model contains the array of 15 receivers above blind fault, the array of 15 receivers in the deep part of the basin and 4 additional receivers at the bedrock. The material parameters of the model are presented in the terms of 1D velocities and density profiles located in the middle part of the shallow and the deep part of the basin. For the corresponding 1D velocity profiles the theoretical dispersion curves for 3 Rayleigh modes are plotted.

Post-processing part of the ASV tool
Multiple stations method - $f-k$ analysis

We present the results of f-k analysis for passive ASV experiment. We used beamforming method for high-resolution three-component beam forming based on Capon (1969). In this case the post-processing was done in the software Geopsy (Wathelet et al. 2018, Wathelet et al. 2020).

The 2 noise sources - receivers configurations (Fig. 8 & Fig. 9) and 1000 realizations of spatial and temporal properties of noise sources were assumed. This resulted in 1000 noise seismograms for each receiver in the presented arrays of receivers. For post-processing purposes the set of 1000 seismograms where considered as the 1000 separated time window slices of one long noise recording.

We extracted the dispersion and ellipticity curves from noise seismograms and plotted them in the colour scale (Fig. 13) based on the values of probability energy density of velocity and ellipticity, respectively. We have also plotted the theoretical Rayleigh surface Modes of dispersion and ellipticity curves for the 1D model of shallow & deep part of the basin. The black straight solid $k_{min}/2$ and dashed k_{max} line in the plots of dispersion curves denote the resolution and aliasing limit based on the geometry of selected receivers (Wathelet et al. 2008), respectively.

In the Fig. 11, the beamforming method was used on the array of all 15 receivers in the deep part of the basin. In the Fig. 12, the beamforming method was used on the sequence of arrays consisting 6, 15, 6 receivers based on their position with respect to the blind fault.
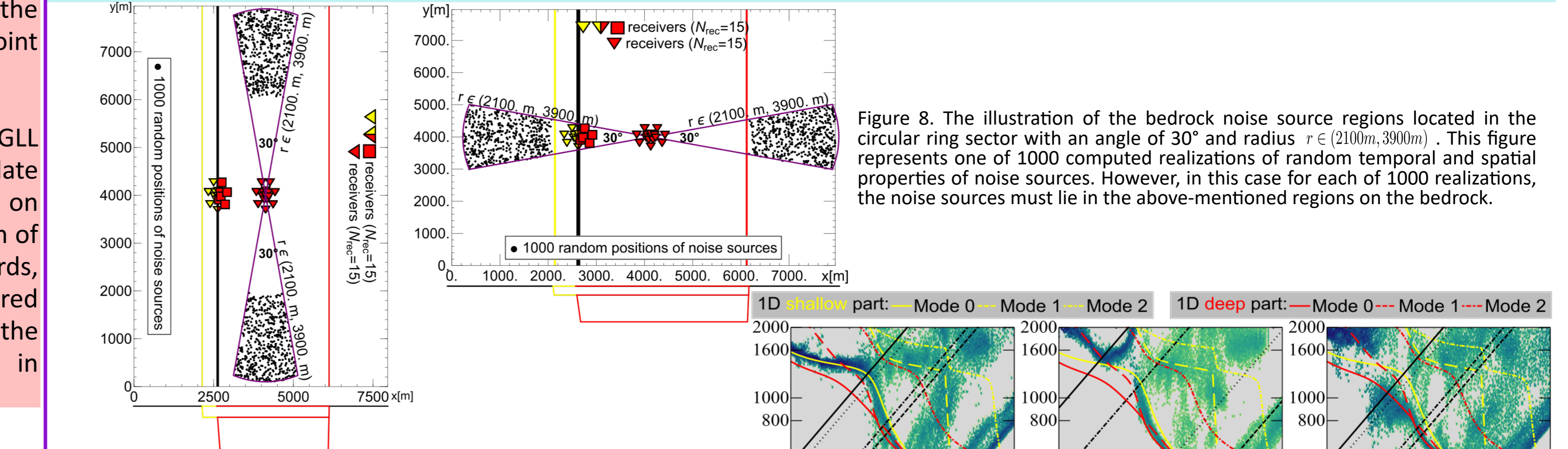

Figure 8. The illustration of the bedrock noise source regions located in the circular ring sector with an angle of 30° and radius $r \in (2100m, 3900m)$. This figure represents one of 1000 computed realizations of random temporal and spatial properties of noise sources. However, in this case for each of 1000 realizations, the noise sources must lie in the above-mentioned regions on the bedrock.

Figure 9. The illustration of the basin noise source regions located in the circular ring sector with an angle of 30° and radius $r \in (2100m, 3900m)$. This figure represents one of 1000 realizations of random temporal and spatial properties of noise sources. However, for each of 1000 realizations, the noise sources must lie in the above-mentioned regions in the basin.

Figure 11. The results of the f-k analysis applied to the array of 15 receivers in the deep part of the basin. In the first column the dispersion curves & ellipticity were extracted from noise seismograms due to noise sources located in the right and left part of the bedrock (Fig. 8). In the second column the dispersion curves & ellipticity were extracted from noise seismograms due to noise sources located in the upper and lower part of the basin (Fig. 9). In each panel we plot also the first 5 theoretical Modes of dispersion curves or ellipticity corresponding to 1D profile in the deep and shallow part of the basin. The straight black solid and dashed line in the first row panels represent resolution and aliasing limit, respectively.
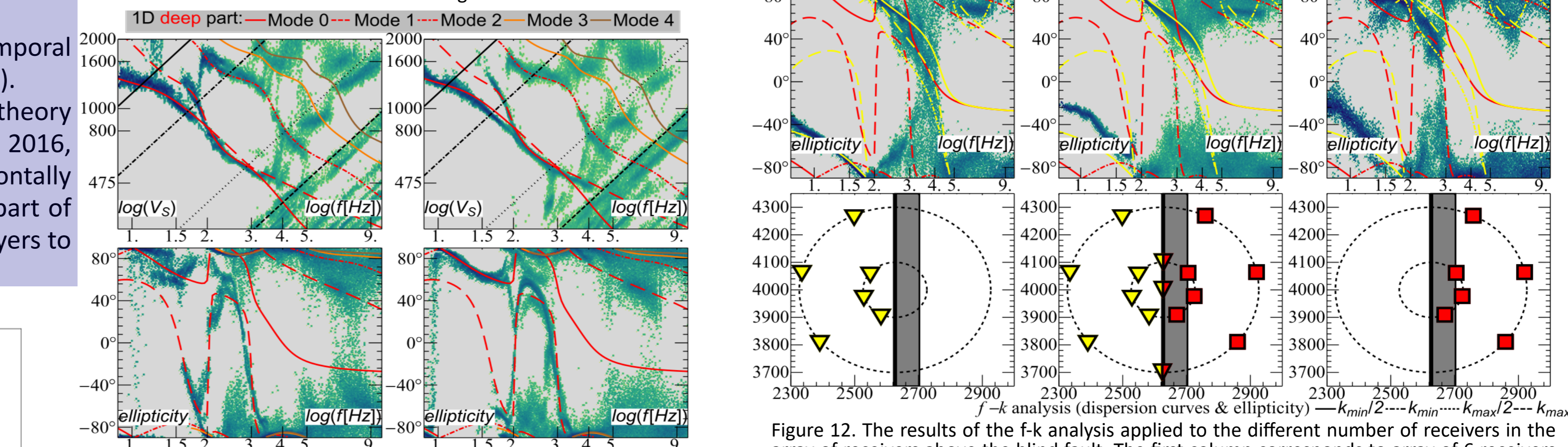

Figure 12. The results of the f-k analysis applied to the different number of receivers in the array of receivers above the blind fault. The first column corresponds to array of 6 receivers located only in the shallow part of the basin. The second column corresponds to the complete array above blind fault with total of 15 receivers. The third column corresponds to array of 6 receivers located only in the deep part of the basin. The corresponding array geometries are pictured in the third row, together with the indication of the projection of the blind fault (black vertical line) and its slope (gray area) on the free-surface. In the first row we present extracted dispersion curves of Rayleigh surface waves from noise seismograms while in the second row we present extracted ellipticity. In each panel we plot also the first 3 theoretical Modes of dispersion curves or ellipticity corresponding to 1D profile in the deep and shallow part of the basin. The straight black solid and dashed line in the first row panels represent resolution and aliasing limit, respectively. For all 3 arrays of receiver, the same noise source regions with 1000 realizations were used, the one in Fig 9.
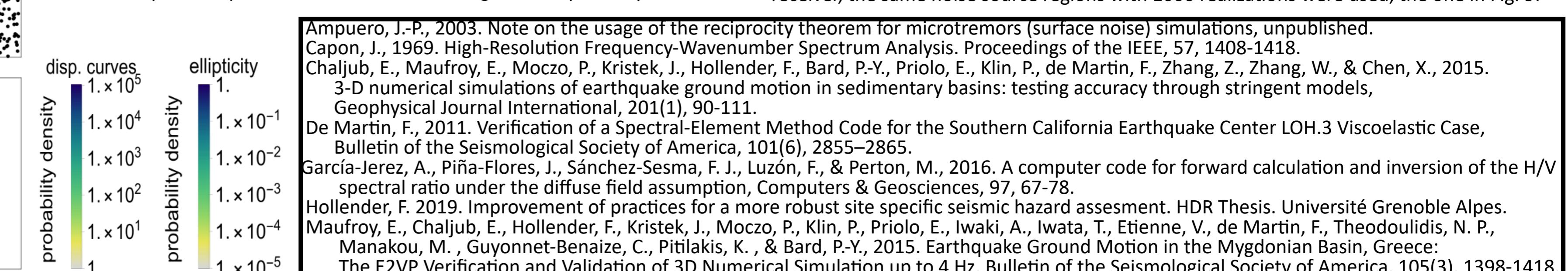

Figure 13. The colour scale of probability energy density of velocity and ellipticity used in Fig.11 & 12.

References:

Ampuero, J.-P. 2003. Note on the usage of the reciprocity theorem for microtremors (surface noise) simulations, unpublished.
Capon, J., 1969. High-Resolution Frequency-Wavenumber Spectrum Analysis. Proceedings of the IEEE, 57, 1408–1418.
Chaljub, E., Maufroy, E., Moczo, P., Kristek, J., Hollender, F., Bard, P.-Y., Priolo, E., Klin, P., de Martin, F., Zhang, Z., Zhang, W., & Chen, X., 2015. 3-D numerical simulations of earthquake ground motion in sedimentary basins: testing accuracy through stringent models, Geophysical Journal International, 201(1), 90–111.
De Martin, F., 2011. Verification of a Spectral-Element Method Code for the Southern California Earthquake Center LOH.3 Viscoelastic Case, Bulletin of the Seismological Society of America, 101(6), 2855–2865.
García-Jerez, A., Piña-Flores, J., Sánchez-Sesma, F. J., Luzón, F., & Perton, M., 2016. A computer code for forward calculation and inversion of the H/V spectral ratio under the diffuse field assumption, Computers & Geosciences, 97, 67-78.
Hollender, F. 2019. Improvement of practices for a more robust site specific seismic hazard assesment. HDR Thesis. Université Grenoble Alpes.
Maufroy, E., Chaljub, E., Hollender, F., Kristek, J., Moczo, P., Klin, P., Priolo, E., Iwaki, A., Iwata, T., Etienne, V., de Martin, F., Theodoulidis, N. P., Manakou, M., Guyonnet-Benaize, C., Pitilakis, K., & Bard, P.-Y. 2015. Earthquake Ground Motion in the Mygdonian Basin, Greece: The E2VP Verification and Validation of 3D Numerical Simulation up to 4 Hz, Bulletin of the Seismological Society of America, 105(3), 1398-1418
Piña-Flores, J., Perton, M., García-Jerez, A., Carmona, E., Luzón, F., Molina-Villegas, J. C., & Sánchez-Sesma, F. J., 2017. The inversion of spectral ratio H/V in a layered system using the diffuse field assumption (DFA), Geophysical Journal International, 208(1), 577–588.
Wathelet, M., Chatelain, J.-L., Cornou, C., Di Giulio, G., Guillier, B., Ohrnberger, M., & Savvaidis, A., 2020. Geopsy: A User-Friendly Open-Source Tool Set for Ambient Vibration Processing, Seismological Research Letters, 91(3), 1878–1889.
Wathelet, M., Guillier, B., Roux, P., Cornou, C., & Bonnefoy-Claudet, S., 2018. Rayleigh wave three-component beamforming: signed ellipticity assessment from high-resolution frequency-wavenumber processing of ambient vibration arrays, Geophysical Journal International, 215(1), 507–523.
Wathelet, M., Jongmans, D., Ohrnberger, M., & Bonnefoy-Claudet, S., 2008. Array performances for ambient vibrations on a shallow structure and consequences over inversion, Journal of Seismology, 12, 1-19.

Figure 5. (a) The representative example of non-decimated time series of Green's function belonging to the set of Green's functions which are stored in the file of total size 5.8 TiB. (b) The FIR and IIR filters applied on the Green's function which decimate the time series by factor of 10 and 16, respectively. (c) The comparison of the non-decimated and decimated (by total factor of decimation 160) Green's function. Thanks to decimation, the total size of file is reduced to only 37.1 GiB.